Estuarine, Coastal and Shelf Science 217 (2019) 69–80

Contents lists available at ScienceDirect

Estuarine, Coastal and Shelf Science

journal homepage: www.elsevier.com/locate/ecss

Near-bed cross-shore suspended sediment transport over a meso-macro tidal beach under varied wave conditions

Wenhong Pang[a], Zhijun Dai[a,b,*], Zhenpeng Ge[a], Shushi Li[c], Xuefei Mei[a], Jinghua Gu[a], Huang-Hu[c,**]

[a] State Key Laboratory of Estuarine and Coastal Research, East China Normal University, Shanghai, 200062, China
[b] Laboratory for Marine Geology, Qingdao National Laboratory for Marine Science and Technology, Qingdao, 266061, China
[c] The Key Laboratory of Coastal Science and Engineering, Beibu Gulf, Qinzhou University, Guangxi, 535099, China

ARTICLE INFO

Keywords:
Suspended sediment transport
Suspended sediment concentration
Tide asymmetry
Wave conditions
Meso-macro tidal beach

ABSTRACT

Cross-shore suspended sediment transport (SST) over meso-macro tidal beaches is of great importance to worldwide coastal erosion due to global sea-level rise. A continuous field experiment of about six tidal cycles measuring cross-shore SST near the seabed in different wave conditions was conducted over Yintan Beach, a meso-macro tidal beach to the north of Beibu Gulf, China. The surveyed data, including synchronous hydrodynamics and suspended sediment concentrations (SSC), were collected with three upward Acoustic Doppler Current Profilers (ADCPs), three Tide & Wave Recorders-2050 (RBRs) and three Optical Backscatter Sensors (OBSs). The results indicate that the SSCs in low and moderate wave heights were responsible for variations in cross-shore suspended sediment fluxes (SSF) at Yintan Beach. During moderate wave conditions, a greater average SSC of over 1.89 kg/m^3 and a longer flood tide duration occurred in rising tide compared with falling tide, accompanied by a maximum SSC of 2.67 kg/m^3 and offshore-directed flows due to cross-shore SST induced by tidal asymmetry. For the most landward measurement site at the surf zone, both net cross-shore SSF and maximum cross-shore SSF were larger than that in the offshore measurement sites over moderate wave conditions, which was ascribed to the strong offshore flows (undertow) induced by breaking waves and radiation stress S_{xx} decay.

1. Introduction

Suspended sediment transport (SST), which exchanges sediment between coasts and oceans (Masselink et al., 2008; Dai et al., 2010), plays a vital role in coastal morphology, especially for sandy beaches. The SST gradients induced by hydrodynamics forces and suspended sediment concentrations (SSCs) in a cross-shore direction determine volumetric changes of beach profiles (Jaffe et al., 1984; Puleo et al., 2000; Paphitis and Collins, 2005; Bolaños et al., 2012), which directly result in morphological evolution of the beach. In recent years, with the increase in probability of oceanic events (e.g., storm surges and supertyphoons) (Knutson et al., 2010; Angnuureng et al., 2017) and the resulting widespread coastal erosion around the world (Bird, 1985; Ge et al., 2017; Harley et al., 2017), it is necessary to complete more research on SST, especially near-bed SST in the nearshore of sandy beaches.

Due to the important role of SST on sandy beaches, considerable efforts to explore near-bed SST under combined wave-current actions have been carried out over the past decades (e.g., Stive and Reniers, 2003; Masselink et al., 2007a,b; Castelle et al., 2007; Capo et al., 2009; Almar et al., 2010; Bruneau et al., 2014; Kularatne and Pattiaratchi, 2014; Wesselman et al., 2017). Earlier work suggested that net cross-shore SST over intertidal beaches was determined by the balance between mean and oscillatory components, which were further divided into incident transports and infra-gravity transports (Jaffe et al., 1984). In subsequent years, related investigations have been conducted based on mean and oscillatory components, which were composed of a wave-induced periodic component and a residual high frequency component (Nielsen, 1992), aiming to analyze the SST mechanism (Osborne and Greenwood, 1992a, b; Ogston and Sternberg, 1995; Elgar et al., 2001). For example, Conley and Beach (2003) believed that approximately 60% of measured integrated transport occurs within the first 5 cm of the water column, and there is a reversal in the direction of net SST with height above the seabed due to the increased influence of oscillatory

* Corresponding author. State Key Laboratory of Estuarine and Coastal Research, East China Normal University, Shanghai, 200062, China.
** Corresponding author.
E-mail addresses: zjdai@sklec.ecnu.edu.cn (Z. Dai), mrhuanghu@126.com (Huang-Hu).

https://doi.org/10.1016/j.ecss.2018.11.007
Received 14 March 2018; Received in revised form 9 July 2018; Accepted 10 November 2018
Available online 12 November 2018
0272-7714/

transport in relation to the seabed. Additionally, Cartier and Héquette (2015) noted that the vertical SSC distributions were related to bar-trough topography because surf bores propagated landward over bar crests and induced an increase in sediment concentration at higher elevation above the bottom in the adjacent trough. However, few studies have been carried out on variations in cross-shore SST from nearshore to surf zones during different tidal cycles superimposed on low or moderate wave conditions.

Many factors, including incident wave conditions, bedform, tidal range and beach gradient, have important influences on variations in near-bed SST, thus, control the morphological changes over a sandy beach (Masselink et al., 2006; Miles and Thorpe, 2015; Pan and Fairbairn, 2016). In low to moderate wave conditions, bar buildup and onshore bar migration (Sunamura and Takeda, 1984) were ascribed to near-bed onshore SST in the form of a 3-dimensional cell circulation across the bar crest under the impact of shoaling incident waves (Aagaard et al., 1998, 2006). In such wave conditions, the bar gradually migrated onshore and welded to the beach face until the runnel landward of the bar crest was infilled. As a result, offshore-directed SST occurred in the form of vertical offshore-directed undertow circulation instead of a 3-dimensional cell circulation (Aagaard et al., 1998, 2006; Masselink et al., 2008; Poate et al., 2014). In contrast, large offshore-directed SST occurs when a storm event encounters a beach, which leads to rapid bar flattening and offshore bar migration (Gallagher et al., 1998; Capo et al., 2009) due to high wave energy swash and surf zone processes (Aagaard et al., 2012). In addition, Miles and Thorpe (2015) suggested that bedforms contributed to the cross-shore sediment transport on a dissipative beach. Specifically, the fractional contribution of cross-shore bedform transport was up to 15% of the total cross-shore transport in the region of breakpoint. Moreover, the joint influence of tide range and beach gradient on SST and the resulting beach morphological changes can be reflected by tidal translation rates and the duration of wave processes over neap to spring tides and micro-to macro-tidal ranges (Reichmuth and Anthony, 2007). The larger the local tidal translation rate is, the shorter the duration of wave processes would be as the water levels shift, which leads to limited cross-shore SST and the resulting morphological response (Davis et al., 1972; Anthony et al., 2004; Reichmuth and Anthony, 2007).

However, while studies referring to hydrodynamics, sediment transport and associated beach morphological evolution over sandy beaches have increasingly received the concern of the world (Masselink and Pattiaratchi, 2000; Dai et al., 2004; Masselink and Russell, 2006; Dai et al., 2007; Austin et al., 2009; Pereira et al., 2013, 2014; Kularatne and Pattiaratchi, 2014), few studies concerning near-bed SST in nearshore to surf zones have been reported in meso-macro tidal beaches of international fields, especially in China. Therefore, a detailed unique field survey, including synchronous hydrodynamics and SSC under low-energy and moderate wave conditions over approximately six tidal cycles, was taken on a meso-macro tidal sandy beach, located in the north of the Beibu Gulf, China. The main objectives of this paper are: i) to explore cross-shore SST under varied wave energy conditions, ii) to examine SST variations during flood and ebb period, and iii) to compare the spatial variabilities of SST.

2. Data and methods

2.1. Study area

The studied region is located at Yintan Beach, north of the Beibu Gulf (Fig. 1). The alongshore sandbar of the beach is oblique to the latitudinal direction, with an angle of approximately 25°. There are multi-sandbar systems developed in the subtidal zone, which can effectively protect the beach face from erosion during the storms. Semi-diurnal and diurnal tides operate alternately over neap and spring, with a mean spring tide range of 3.6 m. The maximum tidal range in spring tides can be up to 5.36 m, while during spring tide, the mean velocity of flood and ebb tidal current is 0.13 m/s and 0.31 m/s, respectively (Huang et al., 2011). The mean wave height in this region is approximately 0.5 m, with seasonal changes (Zhou et al., 2015). Typhoons pass over this region occasionally from June to October, inducing storm surges. Due to the impacts of the southwest monsoon, the wave direction is northward in winter and southwest wave in summer. Moreover, beach sediments mainly consist of unconsolidated quartz sands and the median grain size above the mean low water level of spring tides varies from 0.14 mm to 0.19 mm, according to previous studies (Huang et al., 2011; Ge et al., 2017).

2.2. Instrument deployment

A continuous field experiment lasting six days, from 22 June to 28 June in 2014, was conducted in the region with approximately six tidal cycles from neap-to- spring tide. Three survey gauging stations (Site A, B, and C) were established to measure waves, currents, and SSCs, which located in cross-shore transects across the inner nearshore zone (Fig. 2). Specifically, $x = 0$ indicates the location of the beach foredune and Site A, Site B, and Site C are approximately 250 m, 420 m, and 570 m away from the beach foredune, respectively (Fig. 2a). At the same time, the elevation differences between two adjacent instrument sites were 2.2 m and 0.3 m. The measurements were taken by upward Acoustic Doppler Current Profilers (ADCP) (Workhorse Sentinel, Teledyne RD Instruments, San Diego, USA), Tide & Wave Recorders-2050 (RBR) (Company, RBR Ltd, Ottawa, Canada), and Optical Backscatter Sensors (OBS) (OBS-3A, D&A Instrument Company, Washington, USA). The equipment of Site A was fixed at the depth of 1 m below mean water level, which means that Site A was submerged intermittently as the tide level varied. However, the instruments in the other two stations were always submerged even at spring low tide levels (Fig. 2).

In Site A, the aluminum frame consisted of one RBR and two OBSs (Fig. 2b). Specifically, the probe of the RBR was mounted 0.2 m above the bed to measure the wave heights, wave periods, and water depths. The RBR was logged at 4 Hz over a consecutive 256-s period at each 10-min interval. Two OBSs were fixed to a vertical-piece of the aluminum frame with their probes located at 0.21 m and 0.86 m above the bed surface, which obtain the turbidity signals and water depths (the upper OBS is ignored here). The OBS was logged at 1 Hz and then the outputs were averaged for every two minutes. Meanwhile, an upward-directed 1200 K-Hz ADCP was inserted into the seabed with its probe 0.11 m above the bed in order to obtain the vertical current velocity. Its blanking distance is 0.22 m, and each measurement cell is 0.1 m. Moreover, the ADCP was logged at 2 Hz, and the current data outputs were averaged over each 2-min interval.

Meanwhile, in Site B and C, identical instruments including RBR, OBS and ADCP were fixed on the aluminum quadripods using the same methods with the same parameter settings. The parameter settings of all the instruments in Site B and Site C (Fig. 2c) were completely the same as those of Site A. However, the probes of OBSs in Site B and C were deployed at a height of approximately 0.4 m (Fig. 2c). Meanwhile, the probes of ADCPs in Site B and C were both approximately 0.4 m above the seabed at the start of the field experiment. Moreover, a 3-dimensional laser scanner (Riegl VZ-4000, RIEGL Company, Horn, Astria) with precision of millimeter was fixed on the foredune of Yintan Beach (Fig. 2a and d) to acquire the variations in beach profile from 24th to 28th June 2014, which was perpendicular to longshore sandbar and passed through Site A.

The pressure sensors and current meters were calibrated prior to deployment, and the sensors of OBSs were calibrated in a cylinder of sediment procured from the deployment location. We used the first-cell horizontal velocity of ADCP to present the near-bed flow velocity in this study. In addition, all the hydrologic instruments were time-synchronized by a computer before the implement of the field experiment, and they operated as self-contained units for long-term observation. Hence, the magnitude of temporal resolution was in the order of minutes for

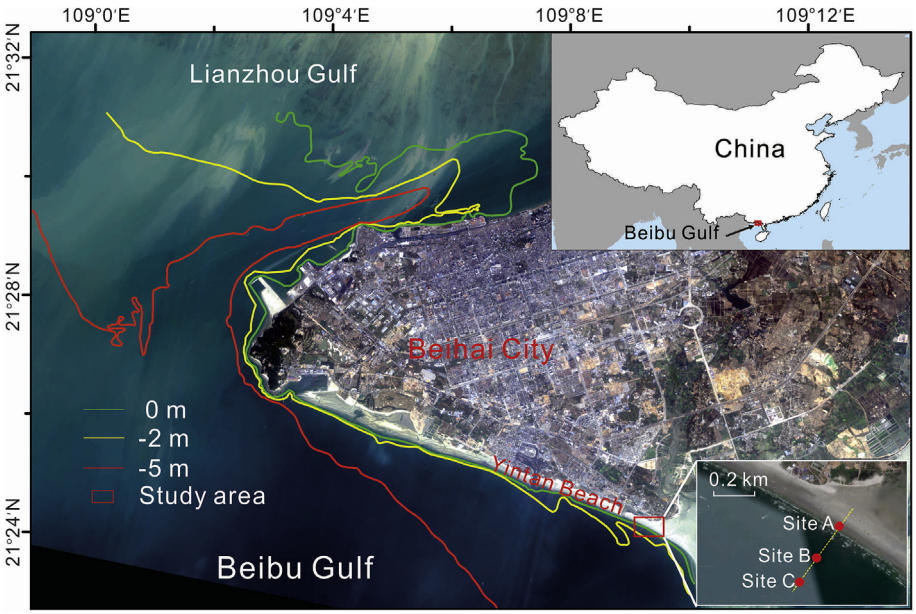

Fig. 1. Study location.

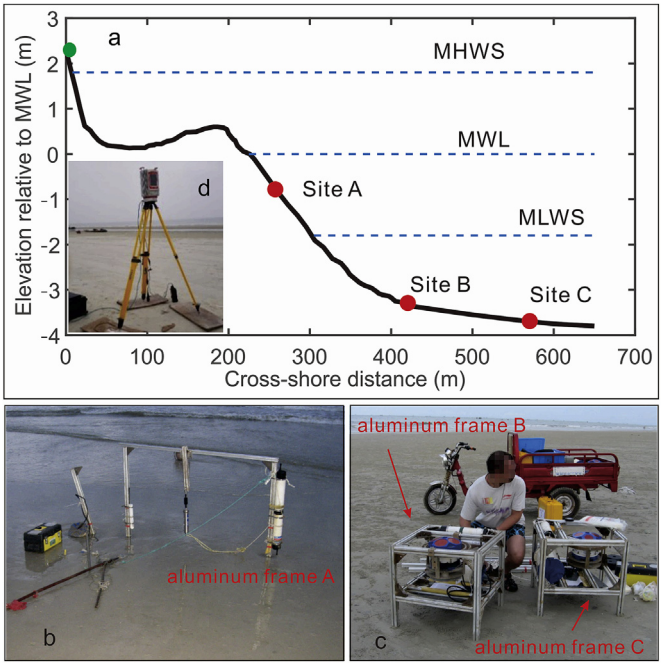

Fig. 2. (a) Beach profiles of Yintan Beach at the beginning of the experiment and locations of experiment sites, with the dashed lines indicating mean high water of spring (MHWS), mean water level (MWL) and mean low water of spring (MLWS), respectively, and the green solid circle indicates the location of the 3-d laser scanner; (b) and (c) indicates the aluminum frame of Site A, Site B and Site C; (d) indicates the 3-dimensional laser scanner. (For interpretation of the references to colour in this figure legend, the reader is referred to the Web version of this article.)

approximately six tidal cycles.

2.3. Data processing and methods

2.3.1. Calibration of OBS

There is no constant proportionality factor between the turbidity signals from OBSs and SSC (Bunt et al., 1999; Sutherland et al., 2000). The OBS sensor gain can vary by a factor of up to 200 with different sediment sizes (D&A Instrument Company, 1991). As a result, it is necessary to calibrate the three OBS sensors separately with the sediment collected at the surface of the instrument location. Therefore, the calibration of the OBS in the laboratory was carried out by fixing the OBS in a cylinder (height, 0.55 m; diameter, 0.35 m) filled with stirring water. Sediment and water were added to the cylinder continuously until the turbidity values were relatively stable for approximately 1 min. Then, suspended sediment measurements were taken with water sampling bottles. Afterwards, the suspended sediment water samples were sent to the Suspended Matter and Salinity Analysis Lab in the State Key Lab of Estuarine and Coastal Research of ECNU, China to calculate the SSC. Eventually, linear least-squares fits were adopted to compute the relationship between turbidity values and corresponding SSC of the water samples. Here, a linear fitting R^2 value varying from 0.991 to 0.997 for the three OBS probes was produced (Fig. 3).

2.3.2. Degree of turbulence of the flow

Defined as the ratio between the inertia forces and viscous forces, the wave Reynolds number, one form of the Reynolds number, is used to measure the degree of turbulence of the flow. According to Boyd et al. (1988), the wave Reynolds number, N_r, is defined as:

$$N_r = {U_m d_0}/{2\nu} \quad (1)$$

where ν is the kinematic viscosity (approximately 10^{-6} m^2s^{-1}), and U_m is wave maximum orbital velocity, which is calculated by linear theory (Nielsen, 1981) or by linear relation with standard deviation of cross-shore current (Masselink and Pattiaratchi, 2000; Sherman and Greenwood, 1984; Aagaard et al., 2012). U_m is calculated as:

$$U_m = {\pi H_s}/{T_s \sinh\left({2\pi h}/{L}\right)} \quad (2)$$

where T_s is the significant wave period, H_s is the significant wave height, h is the water depth and L is the wave length. L can be calculated by iterative computations through the linear wave dispersion relation:

$$L = {gT^2}/{2\pi} \tanh {2\pi h}/{L} \quad (3)$$

In equation (1), d_0 is the near-bed orbital diameter, which is equal to two times of orbital semi-excursion A, and A was obtained by:

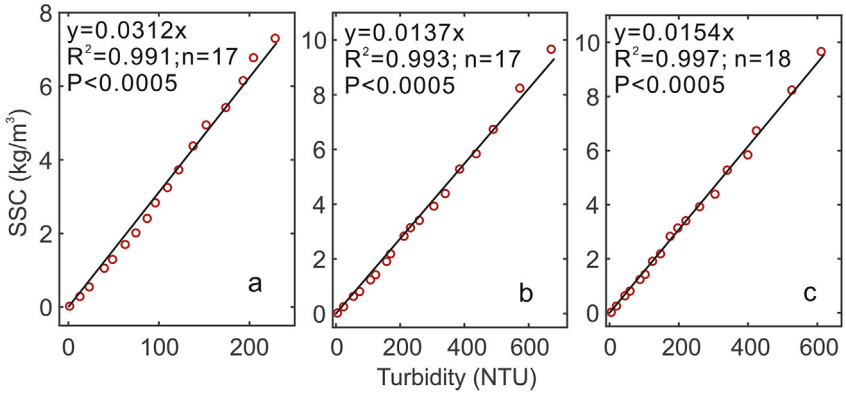

Fig. 3. Linear least-squares fits between turbidity value and SSC of the water samples for (a) Site A, (b) Site B and (c) Site C.

$$A = {U_m T}/{2\pi} \tag{4}$$

2.3.3. Parameters associated with suspended sediment transport

The net cross-shore SSF (< F >) was composed of mean and oscillatory components (Jaffe et al., 1984):

$$<F> = \bar{u}\bar{c} + <\acute{u}\acute{c}> \tag{5}$$

where $\bar{u}\bar{c}$ denotes the time-averaged quantities of SSF caused by mean current over wave periods. $\acute{u}\acute{c}$ is obtained as the product of the oscillatory SSC ($\acute{c}$) multiplied by oscillatory current velocity ($\acute{u}$).

For the oscillatory motion, incident wave period is less than 25 s and infra-gravity wave period is usually defined between 25 s and 250 s (0.004 < frequency < 0.04) (Elgar et al., 1992). However, since the time series of SSC (c) and cross-shore current velocity (u) are both on the time scale of 2 min by averaging the original data with the embedded programs, we estimated the < F > by:

$$<F> = \bar{u}\bar{c} \tag{6}$$

where $\bar{u}$ and $\bar{c}$ are taken averaged every 2 min.

To compare the potential ability of near-bed SST in different sites, normalized SST ability (q^*) is made following Conley and Beach (2003):

$$q^* = {\bar{u}\bar{c}}/{\rho(U_m + <V>)} = {<F>}/{\rho(U_m + <V>)} \tag{7}$$

where < V > is the time-averaged total current velocity on the time scale of 10 min, in accordance with wave data. The normalization relates the SST to the maximum fluid momentum because $\rho(U_m + <V>)$ is on behalf of the fluid potential for the SST. Larger absolute values of q^* indicate stronger SST, and the positive/negative values indicate onshore/offshore direction.

The normalized velocity skewness (U_{SK}) is introduced to predict the direction of SST under different wave energy conditions, though the normalized velocity skewness cannot predict the magnitude of the SSF. Defined by Wells (1967), U_{SK} is obtained as the ratio between velocity skewness $<u^3>$ and velocity variance $<u^2>^{1.5}$ (Masselink and Russell, 2006):

$$U_{SK} = {<u^3>}\Big/{<u^2>^{1.5}} \tag{8}$$

where the angle brackets denote the time average, and the data point of U_{SK} was obtained once an hour through average calculation.

2.3.4. Calculation of bed shear stresses due to wave and current

The bed shear stress due to current (τ_c) was obtained following van Rijn (1993) defined as:

$$\tau_c = \rho_w u_{*c}^2 \tag{9}$$

where ρ_w is the density of seawater (1025 kg/m^3), and u_{*c} is the friction velocity which was estimated according to Fang and Ichiye (1983) as follows:

$$u_{*c} = \frac{\kappa \overline{u_h}}{\ln(4h/z_0) - {8}/{3}} \tag{10}$$

where κ = 0.40 is Von Karman's constant, h is the water depth, z_0 is the bed roughness length which is related to median grain size, D_{50} (D_{50} = 0.144 mm, 0.125 mm and 0.105 mm at Site A, Site B and Site C, respectively), as $z_0 = D_{50}/12$, and $\overline{u_h}$ is the depth-averaged velocity which is calculated following Soulsby (1997):

$$u_z = \begin{cases} \left(\frac{z}{0.32h}\right)^{\frac{1}{7}} \overline{u_h} & 0 < \frac{z}{h} < 0.5 \\ 1.07\overline{u_h} & 0.5 < \frac{z}{h} < 1 \end{cases} \tag{11}$$

where u_z is the flow velocity at the elevation of z.

The bed shear stress due to wave (τ_w) was calculated by the following equation (Fredsoe and Deigaard, 1992):

$$\tau_w = \frac{1}{2}\rho_w f_w U_m^2 \tag{12}$$

where ρ_w is the density of seawater, U_m is the wave maximum orbital velocity obtained in Equation (2), f_w is the wave friction factor and it was estimated following Swart (1974) as:

$$f_w = \exp\left[5.213\left(\frac{k_s}{A}\right)^{0.194} - 5.977\right] \tag{13}$$

where A is near-bed orbital semi-excursion, k_s is the bed roughness height given by 2.5 D_{50}.

In addition, the critical bed shear stress (τ_{cr}) for initiation of sediment motion was obtained following Soulsby (1997) as:

$$\tau_{cr} = \theta_{cr}(\rho_s - \rho_w)gD_{50} \tag{14}$$

where ρ_w and ρ_s are the density of seawater (1025 kg/m^3) and quartz grain (2650 kg/m^3), respectively, D_{50} is the median grain size, θ_{cr} is the critical Shield's parameter for initiation of sediment motion which was obtained from Soulsby (1997) as:

$$\theta_{cr} = \frac{0.24}{D_*} + 0.055[1 - \exp(-0.02D_*)] \tag{15}$$

where D_* is the dimensionless grain diameter given as:

$$D_* = \left[\frac{g(s-1)}{\nu^2}\right]^{\frac{1}{3}} D_{50} \tag{16}$$

where s = 2.59 is the ratio of density of quartz grain and density of seawater as given in Equation (14), ν is the kinematic viscosity of seawater (approximately be equal to 1.0×10^{-6} m^{2}s^{-1}).

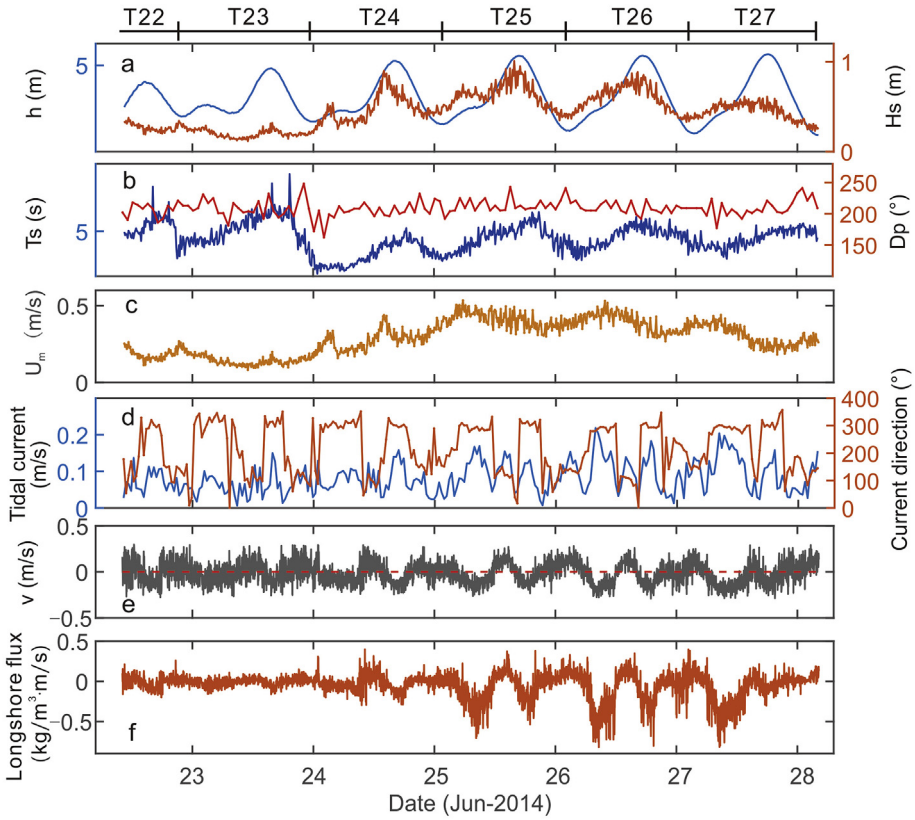

Fig. 4. Time series of (a)water depth h and significant wave height Hs; (b) significant wave period T_S and peak wave direction D_p; (c) maximum wave orbital velocity U_m; (d) magnitude and direction of tidal current; (e) longshore flow velocity v; (f) longshore flux of suspended sediment in Site C. The data point involving flow velocity is averaged for every two minutes and the data point involving wave is averaged for every ten minutes while those involving tide current is averaged for every half an hour.

3. Results

3.1. Characteristics of shoaling hydrology

The hydrodynamic characteristics in the shoaling zone of the Yintan Beach between 22 June and 28 June 2014, can be represented by the measured data in Site C (Fig. 4). The field experiment started from an incomplete neap tide, with a tide range less than 1.6 m and ended in a spring tide with a range of 3.63 m. In view of tidal type, irregular semidiurnal tide and regular diurnal tide were experienced in turn (Fig. 4a).

The H_s varied from 0.12 m to 0.38 m during neap tide from T22 to T23 (T22, T23, T24, T25, T26 and T27 referred to the tidal cycle with high tide on 22nd, 23rd, 24th, 25th, 26th and 27th of Jun 2014 hereinafter) and then increased quickly to 0.9 m at the high tide during T24 (Fig. 4a). Accordingly, the Yintan Beach was subjected to two different wave conditions: low-energy wave conditions ($H_s < 0.5$ m) with tidal cycle-averaged $H_s = 0.2$ m, T_s ranging from 4.0 to 6.5 s and moderate wave conditions (0.5 m $< H_s <$ 1 m) with tidal cycled-averaged H_s close to or greater than 0.5 m and T_s ranging between 3.1 and 6.5 s (Table 1). The results of the peak wave directional spectrum D_p showed that the dominant incident wave angles were mainly approximately 209° (Fig. 4b). Moreover, based on Eq. (2), the maximum wave orbital velocity U_m changed synchronously with H_s, and its minimal value was as small as 0.08 m/s and increased up to 0.53 m/s at the moderate wave conditions on T25 (Fig. 4c).

The velocity of tidal current ranged from 0.005 m/s at slack water to 0.15 m/s at flood tide during neap tide, while stronger tidal current occurred during flood and ebb tide of spring tides, with its maximum current velocity increasing up to 0.22 m/s on T26 (Fig. 4d). Specifically, the flood tidal current was generally greater than ebb tidal current. The mean flood tidal current was up to 0.10 m/s and mean ebb tidal current was equal to 0.08 m/s, respectively. Accordingly, the mean direction of flood current was approximately 323° (0° indicates northward) while the mean direction of ebb current was 153° (Fig. 4d), which indicates axial misalignment between flood current and ebb current. In addition, by calculating the coefficient of flow dominance (defined as tidal excursion due to ebb tide divided by the sum of tidal excursions due to ebb and flood tides) (Simmons, 1955), the resulting dominance coefficient was 35%. Thus, it is flood dominant in terms of tidal asymmetry over Yintan Beach.

Most of the longshore flow velocity varied from −0.25 m/s to +0.25 m/s, with its maximum approaching 0.3 m/s and it showed regular variations as the changing tidal level changed (Fig. 4e). Moreover, weak longshore suspended sediment flux occurred before T24, while strong longshore flux occurred during T25, T26 and T27 with their magnitude up to 0.75 kg/m^3·m/s (Fig. 4f). However, we focused on cross-shore suspended sediment transport in the study, though longshore sediment transport prevailed during moderate wave conditions and to some extent affected the cross-shore sediment transport (Beach and Sternberg, 1992), which need further work in the future research.

3.2. Suspended sediment transport in varied wave conditions

The measured and calculated data of Site C were used to analyze the SST in varied wave conditions. During T23, when the Yintan Beach was subjected to low-energy wave conditions, the corresponding N_r, and A were relatively small within range of $0.20 \pm 0.09 \times 10^5$ and 0.12 ± 0.11 m, respectively (Fig. 5 a-1, Table 1), indicating weak flow turbulence. The cross-shore velocity u was characterized by 8.25 ± 9.72 cm/s (Table 1), which is rather small, with a positive

Table 1
Tidal cycle-averaged hydrodynamic parameters, SSC and < F > for the five complete tide cycles from neap to spring tide.

	T23	T24	T25	T26	T27
	Ave±Std	Ave±Std	Ave±Std	Ave±Std	Ave±Std
TR (m)	2.27	2.95	3.30	3.48	3.50
Hs (m)	0.20±0.04	0.47±0.15	0.62±0.14	0.59±0.14	0.44±0.10
E (J/m^2)	28.73± 12.37	160.94± 105.75	277.19±117.70	137.15±112.14	137.15±53.98
N_r (×10^5)	0.20±0.09	0.63±0.32	1.52±0.40	1.39±0.41	0.83±0.32
u (cm/s)	8.25±9.72	−0.76±7.84	−9.46±6.91	−15.74±7.59	−13.89±8.76
SSC (kg/m^3)	0.43±0.14	0.80±0.27	1.43±0.73	1.61±0.75	1.11±0.76
F (kg/m^3•m/s)	3.44	0.73	−7.54	−19.97	−12.43

Note: T23 (24, 25, 26, 27) indicates that the high tide respectively occurs on 23 (24, 25, 26, 27) of June.

mean value in the onshore direction. The mean SSC in the near bed (0.4 m above the seabed) was as small as 0.43 kg/m^3 and fluctuated within the same order of magnitude (Table 1). Further, the mean cross-shore SSF also had small oscillations, varying mostly from −0.1 to 0.1 kg/m^3·m/s and was limited by a small SSC in the water column (Figs. 5 a-3). The < F > in this tidal cycle was equal to 3.44 kg/m^3·m/s, indicating onshore-directed SST, which agreed well with previous work of Masselink et al. (2008) under low wave conditions. It is also noted that there was 4% of q* located outside ± 6 × 10^{-5} with a maximum absolute value less than 1 × 10^{-4} under low-energy wave conditions (Fig. 5 a-5). In summary, during T23, when low-energy wave conditions prevailed, flow turbulence intensity was weak, and SSCs were small with an equivalent magnitude of variation range. Moreover, the sediment transport ability of flow was relatively weak though a small amount of onshore-directed < F > occurred.

T24 was a transitional period, after which the beach was subjected to moderate wave conditions (Fig. 4a). The tidal cycle-averaged H_s was 0.47 m, and the T_s decreased to a range of 3.0–5.0 s (Fig. 4b). Both N_r and A increased rapidly due to the increasing of H_s. u was −0.76 ± 7.84 cm/s, which suggested that the mean components of flows were negligible. The mean SSC was 0.80 kg/m^3 (Table 1), and < F > was insignificant at 0.73 kg/m^3·m/s.

During T25, when the moderate wave conditions prevailed, the tidal cycle-averaged N_r was 1.52 × 10^5, which meant the degree of turbulence of flow caused by the coupling between moderate wave conditions and medium-to-spring tide ranges was significantly higher than that during T23. Specifically, the time series of u was located in −9.46 ± 6.91 cm/s (negative value represents off-shore direction), which was significantly different from that during T23 (Table 1). At the same time, the averaged SSC was approximately 3 times as large as that of T23, with a maximum SSC of 4.1 kg/m^3 occurring on the rising tide (Fig. 5 a-3). Additionally, < F > for T25 reversed to be offshore-directed (negative) and was several times larger than that during T23. In view of q* over T25, 9% were located outside of ± 6 × 10^{-5}. In addition, it indicated larger magnitude and more dominated offshore sediment transport compared with T23.

For the other tidal cycles during moderate wave conditions, T26 and T27 presented similar magnitudes of u, SSC and < F > as T25 (Table 1), accompanied by the maximum absolute values of q*, approaching 2 × 10^{-4} at the end of the ebb tide of T26 and at the beginning of flood tide of T27 (Fig. 5 a-5). Moreover, there were two peaks (called 'M' shape, over T25) and even three peaks (over T26) in the time series of SSC during one tidal cycle (Fig. 5 a-3). A similar phenomenon was also observed at Site B.

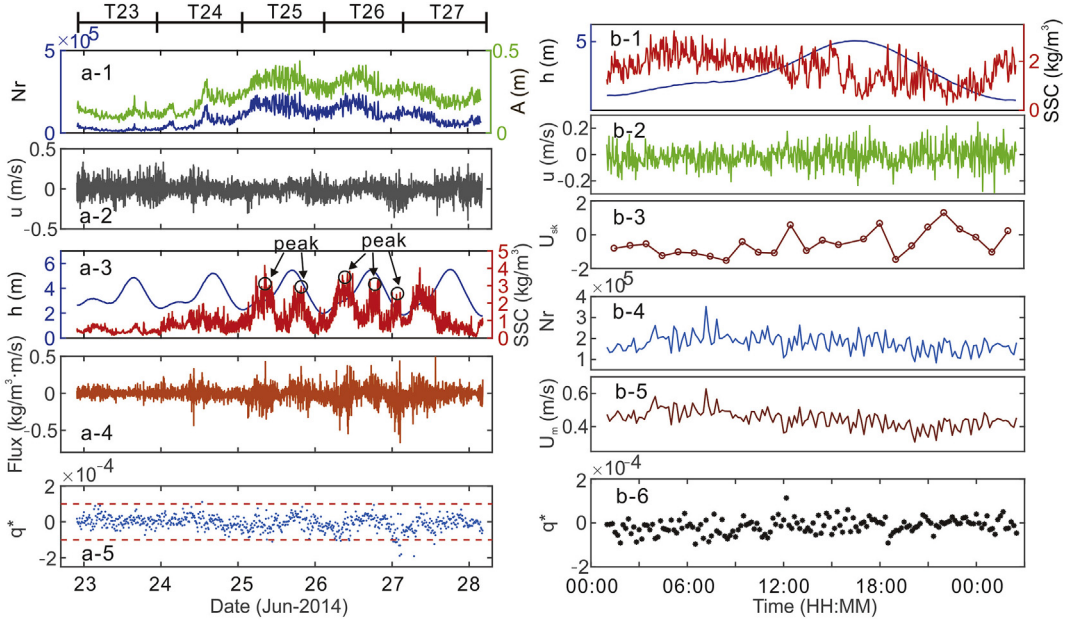

Fig. 5. Time series of hydrodynamic parameters, SSC and normalization of sediment transport ability q* at Site C (left panel) and at Site B during T25 (right panel), respectively, with (a-1) wave Reynolds number Nr (blue line) and orbital semi-excursion A (green line); (a-2) mean cross-shore velocity u; (a-3) water depth h (blue line) and suspended sediment concentration SSC (red line); (a-4) cross-shore suspended sediment flux; (a-5) normalized sediment transport ability q*; (b-1) water depth h (blue line) and suspended sediment concentration SSC (red line); (b-2) mean cross-shore velocity u; (b-3) hourly normalized velocity skewness U_{SK}; (b-4) wave Reynolds number Nr; (b-5) maximum wave orbital velocity U_m; (b-6) normalized sediment transport ability q*. The red dashed lines in (a-5) indicate q* = ±1×10^{-4}. (For interpretation of the references to colour in this figure legend, the reader is referred to the Web version of this article.)

Table 2
Flood-averaged hydrodynamic parameters, SSC and < F > for the five complete tide cycles from neap to spring tide.

	T23	T24	T25	T26	T27
	Ave±Std	Ave±Std	Ave±Std	Ave±Std	Ave±Std
u (cm/s)	−0.21±12.09	0.86±10.47	−1.77±6.70	−1.46±7.33	−1.85±8.06
U_{SK}	−0.04±0.49	0.20±0.91	−0.70±0.71	−0.41±0.99	−0.61±0.57
N_r (×10^5)	0.24±0.10	0.62±0.04	1.90±0.40	1.92±0.45	1.13±0.44
U_m (m/s)	0.15±0.04	0.28±0.06	0.47±0.05	0.47±0.05	0.36±0.07
SSC (kg/m^3)	0.53±0.16	1.01±0.40	1.98±0.46	1.89±0.65	1.79±0.42
F (kg/m^3•m/s)	−1.05	5.02	−16.41	−13.69	−12.97

Note: T23 (24, 25, 26, 27) indicates that the high tide respectively occurs on 23 (24, 25, 26, 27) of June.

3.3. Suspended sediment transport during flood and ebb periods

The phenomenon of tidal asymmetry is ubiquitous for sandy beaches (Masselink et al., 2000). The Yintan Beach is chronically subjected to mixed tides that are composed of irregular semidiurnal tides during the neap tide and regular diurnal tides in the spring tide. Thus, it is meaningful to analyze cross-shore SST of flood and ebb tides, in which we use the measured data from Site B.

The statistical flood-averaged and ebb-averaged hydrodynamic parameters, SSC, and < F > of each tidal cycle are shown in Table 2 and Table 3, respectively. Under the combined influence of tidal currents and waves during rising tide of T23, the SSC maintained a low level characterized by a mean value of 0.53 kg/m^3, with little fluctuation, which led to a small and offshore-directed < F > (−1.05 kg/m^3•m/s). During the flood phase of T24, H_s increased gradually with the decreasing T_s, while < F > turned out to be onshore-directed (5.02 kg/m^3•m/s), in accordance with a positive average u (0.86 m/s). There was high similarity in hydrodynamic parameters and SSC among T25, T26 and T27, with u = -1.77±6.70 cm/s, −1.46±7.33 cm/s and −1.85±8.06 cm/s and SSC = 1.98±0.46 kg/m^3, 1.89±0.65 kg/m^3 and 1.79±0.42 kg/m^3, respectively.

In contrast, during the ebb phases of the experiment, there were relatively significant differences in hydrodynamic parameters, SSC and < F > between low-energy and moderate wave conditions (Table 3). During T23, SSC and < F > were 0.55 ± 0.14 kg/m^3 and -1.88 kg/m^3•m/s, respectively, which behaved so similarly to the flood phases (Table 2) that we came to a preliminary conclusion that the tidal asymmetry in the low-energy wave condition was insignificant. < F > during the ebb phase of T24 was −3.68 kg/m^3•m/s, in the opposite direction compared to the corresponding flood phase. For the ebb phases of the other three tidal cycles, there are obviously smaller values in the averaged H_s, N_r and SSC as compared to those in the corresponding flood phases. Moreover, < F > was much smaller than that during the flood phase; However, it was still in the offshore direction. As we can see, the suspended sediments were continually transported offshore in both flood and ebb phases during the experiment, excluding the flood tide during T24, when H_s was increasing.

Furthermore, the measurement during T25 that was subjected to moderate wave conditions was selected (Fig. 5b) as representative to analyze the tidal-cycle process, when the tide range was 3.3 m and the lunar tidal period was 24.3 h, with the flood duration (15 h) notably longer than ebb tide (9.3 h) (Figs. 5 b-1). The time series of SSC showed a similarly changing pattern with N_r regardless of different values. Specifically, SSC was close to 2 kg/m^3 at the start of the flood, which subsequently reached its peak of 3.34 kg/m^3 in the middle of flood. Then, an obviously decreasing trend was observed until the minimum SSC (0.16 kg/m^3) occurred at the middle of the ebb tide, which was followed by a continuous increase for the rest of the ebb tide (Figs. 5 b-1). Using statistics, 13.8% of q^* were located outside ± 6 × 10^{-5} with the maximum q^* larger than 1 × 10^{-4} during flood tide, whereas only 3.3% q^* were located outside ± 6 × 10^{-5} without a q^* larger than 1 × 10^{-4} (Figs. 5 b-6) during ebb tide. The summation of q^* over flood and ebb tides were equal to −0.00180 and −0.00038, respectively. Overall, stronger offshore sediment transport could be confirmed during the flood phase in terms of q^*. Moreover, similar statistical results of q^* were also found at Site C during T25.

Further, the time series of u, N_r, SSC and cross-shore sediment flux over T25, T26 and T27 were re-sampled and compared to detect the cross-shore SST transport mechanism during moderate wave conditions with an emphasis of asymmetry. In the ensemble tidal process, the normalized time scale of high tide was approximately 0.6, indicating that the flood duration was larger than the ebb duration, which was in agreement with the example of the T25 tidal cycle (Figs. 5 b-1). Both u and cross-shore SSF had more offshore-directed data points with larger values during the flood phase, whereas the data points during the ebb phases showed a relatively uniform distribution (Fig. 6a and c). The time series of SSC showed a similarly changing pattern with N_r regardless of different values (Fig. 6b and d). The peak of SSC (2.67 kg/m^3) occurred in the flood phase when a greater averaged value of 1.89 kg/m^3 was detected, whereas the minimum of SSC (0.61 kg/m^3) existed in the ebb phase. Obviously, both the ensemble and example tidal cycle suggest that the flood phase had a higher degree of flow turbulence intensity and hence a higher SSC in the water column, as well as stronger sediment transport ability than that in the ebb phase (Figs. 5 b-6, Fig. 6). In all, the ensemble tidal processes were consistent with the example tidal process, which means that the example tidal process well represents the averaged tidal cycle in moderate wave conditions.

Table 3
Ebb-averaged hydrodynamic parameters, SSC and < F > for the five complete tide cycles from neap to spring tide.

	T23	T24	T25	T26	T27
	Ave±Std	Ave±Std	Ave±Std	Ave±Std	Ave±Std
u (cm/s)	−1.27±9.54	−1.00±7.20	−0.63±8.49	−1.45±7.43	−1.21±8.15
U_{SK}	−0.46±0.51	−0.30±0.65	−0.07±0.83	−0.39±0.67	−0.65±0.45
Nr (×10^5)	0.25±0.11	0.94±0.29	1.61±0.38	1.37±0.30	0.70±0.23
U_m (m/s)	0.16±0.03	0.34±0.06	0.41±0.04	0.38±0.04	0.27±0.04
SSC (kg/m^3)	0.55±0.14	0.97±0.34	1.23±053	1.29±0.48	1.03±0.33
F (kg/m3•m/s)	−1.88	−3.68	−2.52	−4.49	−3.46

Note: T23 (24, 25, 26, 27) indicates that the high tide respectively occurs on 23 (24, 25, 26, 27) of June.

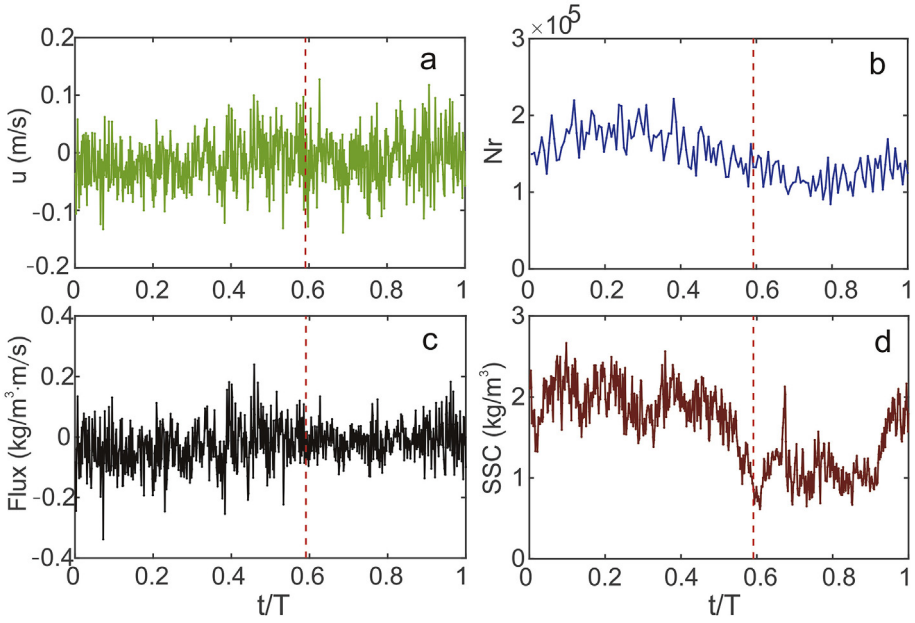

Fig. 6. Statistical tidal cycle-averaged series of (a) mean cross-shore velocity u, (b) wave Reynolds Number Nr, (c) cross-shore suspended sediment flux and (d) SSC during T25, T26 and T27. The vertical dashed line indicates high tide of normalized tidal cycle.

3.4. Spatial variability in suspended sediment transport

To compare the spatial cross-shore SST between the three study sites, the information of hydrodynamics and cross-shore SST in Site A is shown in Fig. 7. The pressure sensors in Site A did not catch the breakpoints because its largest relative wave height, defined as the ratio of H_s to h did not reach 0.78 (Fig. 7a). The H_s in Site A was slightly larger than those in Site B and Site C as a result of the shoaling wave deformation effect (Elgar and Guza, 1985; Certain et al., 2017). By statistics, the majority of u was located between± 0.3 m/s, accompanied by the largest negative velocity occurring in the flood tide at Site A. Therefore, the magnitudes of u in the water column just outside of the surf zone were larger than those in the more offshore zone, especially in moderate wave conditions, such as T25 and T26, which have been approved by previous researchers (e.g., Aagaard et al., 2012). It can be seen in Fig. 7c that the maximum and minimum SSC were 0.16 and 3.08 kg/m^3, respectively, which occurred during the high tide of T23 and in the flood tide of T25. It needs to be noticed that a high SSC occurred both in the beginning of the flood tide and in the end of the ebb tide at Site A. The cross-shore SSFs were large, with its instantaneous maximum offshore-directed value in excess of 0.8 kg/m^3·m/s. Beyond our expectation, q^* ranged ± 0.00005 in low-energy wave conditions (T23 and T24) and ranged between a wider extent of $-0.00015 < q^* < +0.00015$ during moderate wave conditions (T25, T26 and T27) at Site A, which were similar results to those at Sites B and C.

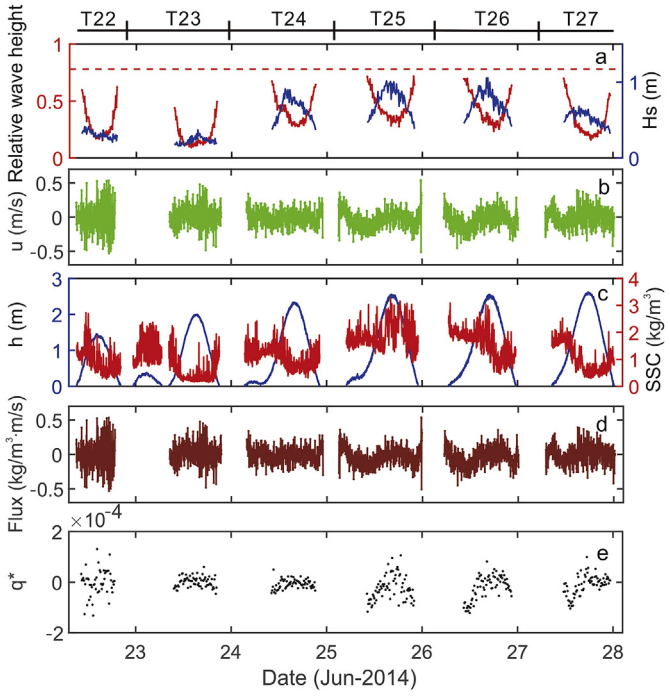

Fig. 7. Time series of (a) relative wave height (red line) and Hs (blue line); (b) cross-shore velocity u; (c) water depth h (blue line) and suspended sediment concentration SSC (red line); (d) cross-shore suspended sediment flux; (e) normalization of sediment transport ability q*. The dotted line in (a) represents the breaking index (relative wave height = 0.78). (For interpretation of the references to colour in this figure legend, the reader is referred to the Web version of this article.)

Fig. 8 listed the < F > over each tidal cycle as 20–40 cm above the seabed as well as offshore tide ranges (TR) and H_s. It can be found that < F > over each tidal cycle under moderate wave conditions was several times larger than that under low-energy wave conditions in all instrument sites, while < F > during moderate wave conditions was an order of magnitude larger than that during low-energy wave conditions in Site A. At the same time, the tidal-cycle < F > under moderate wave conditions were all negative, indicating offshore SST, which could be in an offshore or onshore direction, with small values under calm conditions. In Fig. 8c, it can be found that all of the tidal < F > in Site A were in an offshore direction, except T22, which did not contain complete tidal cycle information. This phenomenon could be explained by the fact that an undertow-induced large mean component dominated the net SST direction around the surf zone, which is consistent with previous findings (e.g. Roelvink and Stive, 1989). Furthermore, < F > in Site A approaching the surf zone was larger than that in offshore areas when the beach was exposed to moderate wave conditions, especially during T25 and T26 (Fig. 8c, d, 8e). Last but not least, < F > values near the seabed over the experiment were −129.38 kg/m^3·m/s, −60.31 kg/m^3·m/s and −36.00 kg/m^3·m/s at Site A, Site B and Site C, respectively, which indicated seaward SST over the field study.

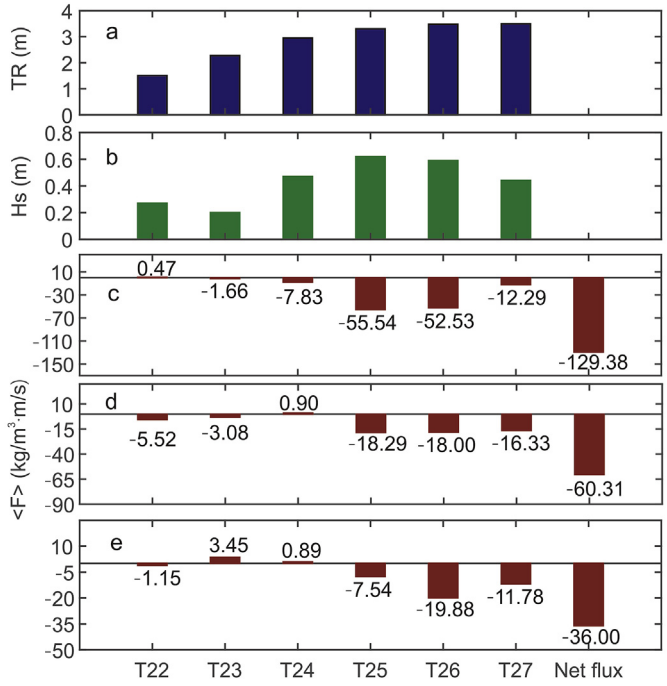

Fig. 8. (a) Tide range TR, (b) Tidal cycle-averaged wave energy, and net cross-shore suspended sediment flux at (c) Site A, (d) Site B and (e) Site C. *Data did not contain complete information over one tidal cycle.

4. Discussion

Waves, current, and beach gradient (topography) could all have some influences on sediment suspension and SSCs of the coastal zone. Here, the potential impacts of possible factors on the near-bed cross-shore SSCs and SST over Yintan are clarified.

During the observation, the beach profile that passes through Site A showed no significant changes in beach gradient (Fig. 9). By statistics, the overall intertidal beach gradients (except foredune) are 8.19‰, 8.25‰, 8.28‰, 8.05‰ and 8.15‰ at low tide, respectively, and the mean beach gradients of lower beach (across Site A) ranged merely from 2.23% to 2.27%. Thus, we inferred that the similar wave

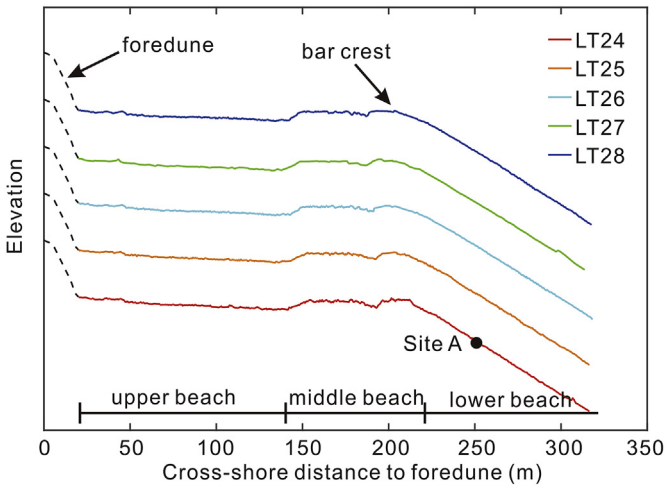

Fig. 9. Intertidal cross-shore beach profiles at low tide during moderate wave conditions. The black filled circle indicates the location of Site A (x = 250 m) at the beginning of the experiment. LT24, LT25, LT26, LT27, LT28 indicate low tide on 24th, 25th, 26th, 27th and 28th of Jun 2014, respectively. The dashed black lines indicate the beach foredune, which can not be acquired from the laser scanner.

dissipation rates occurred during the observation and the almost constant beach gradients have minor impacts on wave reflection and dissipation.

Meanwhile, the role of wave and current on SSC in the water column could be further examined by calculating the bed shear stress due to wave (τ_w), and current (τ_c), respectively (Fig. 10). The results showed that τ_w and τ_c ranged from 0.06 N/m^2 to 1.50 N/m^2 (mean value of 0.50 N/m^2) and from 0.002 N/m^2 to 0.08 N/m^2 (mean value of 0.016 N/m^2) at Site B (Fig. 10b), respectively. Meanwhile, the corresponding shear stresses ranged from 0.05 N/m^2 to 1.11 N/m^2 (mean value of 0.43 N/m^2) and from 0.003 N/m^2 to 0.08 N/m^2 (mean value of 0.018 N/m^2) at Site C (Fig. 10c), respectively. Thus, the sediment motions over Yintan Beach were dominated by wave since τ_w was an order of magnitude larger than τ_c which was noticeably less than τ_{cr}. Besides, at Site A closing to surf zone, the bed shear stress due to wave (ranging from 0.25 N/m^2 to 4.11 N/m^2, mean value of 1.84 N/m^2) was also an order of magnitude larger than that due to current (ranging from 0.005 N/m^2 to 0.30 N/m^2, mean value of 0.04 N/m^2), though the latter became larger than τ_{cr} compared with that at Site B and Site C at very low tide (Fig. 10a).

Moreover, the Yintan Beach encountered two wave conditions during the field experiment, namely, low-energy (lower than 0.5 m) and moderate wave conditions (0.5–1 m). In the latter case, < F > values in the water column (40 cm above the seabed) were several times larger than those in the former case. In addition, the sediment transportability of flow during moderate wave conditions was stronger than that during low-energy wave conditions as confirmed by q* (Fig. 5 a-5), during which SSCs under moderate wave conditions were several times larger than those in low-energy wave conditions (Table 1). By correlation analysis between SSC and H_s at Site B and Site C, the linear correlation coefficients are up to $R^2 = 0.3609$ (n = 830, P < 0.0005) and $R^2 = 0.3659$ (n = 828, P < 0.0005), respectively (Fig. 11). Hence, waves played a vital role in cross-shore SSFs over Yintan Beach. At the same time, u could not account for the SSC in the water column, which has been confirmed by Austin et al. (2009) through the statistical distribution of root mean square of u. Hence, it can be confirmed that SSCs induced by different wave heights, rather than u in the water column, were responsible for variations in cross-shore SSFs at the Yintan Beach. However, for the first crest of SSC in T25 (Figs. 5 a-3), it coincides with the maximum N_r during rising tide because of the large wave-induced high-degree of flow turbulence that can make more sediments spread upward from the bottom by diffusion (Figs. 5 a-1, a-3) (Hanes and Huntley, 1986; Osborne and Greenwood, 1993). However, for the other crests of SSC during the high tide and falling tide, no evidences was obtained to account for their appearance. Thus, wave data can not completely explain the 'M' shape (Figs. 5 a-3) and the three peaks of the SSC time-series over the tidal process. This was similar to the study of Delgado et al. (2015), who assumed that there were two different mechanisms controlling sediment suspension under mild and more energetic wave conditions.

Waves also play an important role in the cross-shore SST, which depends on the balance between the mean component and the oscillatory component. The oscillatory component can be further divided into the incident wave component, the infra-gravity component and turbulent component (e.g. Jaffe et al., 1984; Nielsen, 1992; Thornton et al., 1996; Aagaard et al., 2002). In our study, we can only get parts of information on the infra-gravity-induced oscillatory velocity (0.0083 < oscillatory frequency < 0.004), but cannot obtain information about the incident wave-induced and turbulent sediment transport (oscillatory frequency > 0.04), because the temporal resolution of both u and SSC time series are at the magnitude of 2 min. By analyzing u, we can find that its variation range was almost the same magnitude for each tidal cycle (Table 1), which indicated the stabilization of the infra-gravity waves-induced oscillatory u' (Aagaard and Greenwood, 1995; Kularatne and Pattiaratchi, 2008, 2014). Furthermore, the averaged u (8.25, −0.76, −9.46, −15.74, −13.89 cm/s for

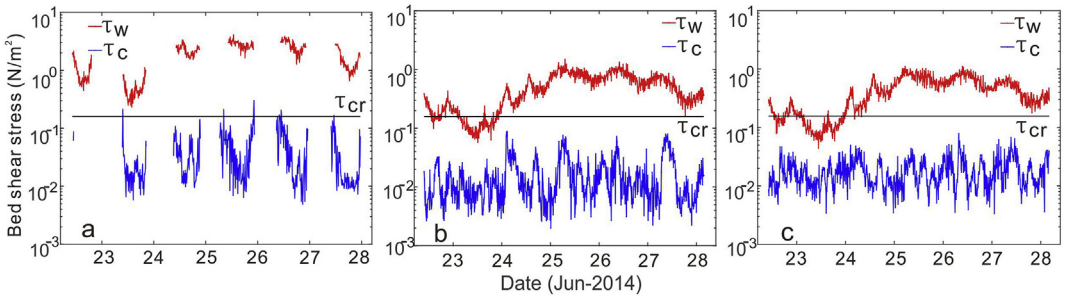

Fig. 10. Calculated bed shear stress due to wave (τ_w) and current (τ_c) in (a) Site A, (b) Site B and (c) Site C, respectively. The horizontal black lines indicated critical shear stress (τ_{cr}) of 0.161 N/m^2, 0.158 N/m^2 and 0.157 N/m^2 in Site A, Site B and Site C, respectively.

T23, T24, T25, T26 and T27, respectively) was significantly linearly correlated with < F > (3.44, 0.73, −7.54, −19.97, −12.43 kg/m^3·m/s for T23, T24, T25, T26 and T27) (Table 1) with correlation coefficient of 0.941 (n = 5, P < 0.001). Thus, it may be hypothesized that the net cross-shore SST was dominated by the mean flow component at an elevation of 40 cm above the bottom over the experiment.

In addition, the small values of negatively averaged u (-0.76 cm/s) correspond to the small values of positive net SSF (0.73 kg/m^3·m/s) during T24 in Site C (Table 1), while a positive averaged u (0.86 cm/s) and a positive net SSF (5.02 kg/m^3·m/s) occurred during the rising tide of the same tidal cycle (Table 2), accompanied by a decreasing T_S (Fig. 4b, ebb tide of T23). The findings is consistent with the study of Grasso et al. (2011) that the decreasing peak wave period will lead to a reverse in sediment transport from being offshore-directed to onshore-directed, as ascribed to the decreasing wave skewness. Generally, sediment resuspension was strongly constrained by the enhanced infra-gravity wave oscillation under the high dissipative conditions (Fig. 4b, large H_s and small T_s) where the infra-gravity component was dominant (Beach and Sternberg, 1988; Butt and Russell, 1999), making suspended sediments available for transport by onshore mean currents.

Extensive studies have been carried out to explore the asymmetry in sediment resuspension in the coastal zone, while tidal asymmetry is conspicuous in the estuary as a result of the relative strength between runoff and tidal power (e.g. Cook et al., 2007; Ridderinkhof et al., 2000; Wang et al., 2013). In an earlier study, Russell et al. (1991) found a distinct asymmetry in strong offshore-directed SST during ebb tide and a much smaller net SST during flood tide. Moreover, Masselink and Pattiaratchi (2000) revealed a pronounced tidal asymmetry that was characterized by a significantly larger SSC and sediment transport rates during the ebb tide than those during the flood tide, which is the result of the coupling of stronger offshore mean flows and greater bed roughness during the ebb tide over a macro-tidal beach. However, during the moderate wave conditions of this study, the peak of SSC occurred during the rising tide, concurrent with the offshore current velocities and longer duration of flood tide. Thus, the magnitude of the resulting < F > (integral of the product of u and SSC) over the flood tide was larger than that over the ebb tide, which predominated the direction of net cross-shore SST over the entire tidal cycle, This was contrary to the findings of Masselink and Pattiaratchi (2000).

The breaking waves and resulting radiation stress have an important influence in the nearshore current systems, especially in the surf zone of sandy beaches (Longuet-Higgins and Stewart, 1964; Greenwood and Osborne, 1990; Xia et al., 2004). Radiation stresses come into being as the incident waves transform and wave energy dissipates with gradually shoaling water depths. As a result, undertow occurs and changes following the varying radiation stress S_{xx}(onshore component of the onshore momentum flux) due to the balance between set-up-induced hydraulic forces, onshore mass fluxes and turbulent stresses induced by wave breaking (Longuet-Higgins and Stewart, 1964). Site A was the most shoreward site in the surf zone considering that its relative wave height nearly approached 0.78 (Fig. 7a). As expected, a smaller u (less than 0.2 m/s for most of time) occurred at Site B and Site C, while a larger u (the majority of u was located between ± 0.3 m/s), up to −0.5 m/s, prevailed at Site A. Thus, it was inferred that the flow velocity in Site A was enhanced by the undertow due to the structure of undertow outside the surf zone (Uday and Svendsen, 2012; Xia et al., 2004), even though the Site A was not completely within the surf zone. On the other hand, strong flow accelerations enhance sediment entrainment from the seabed and lead to higher SSC approaching the surf zone as the waves propagate landward. In addition, SST rates in the inner surf zones should be about one order of magnitudes larger than that under shoaling and weakly breaking waves because of larger SSC in inner surf zones (Aagaard et al., 2002, 2006). However, the tidal cycle-averaged SSCs at Sites C and B were slightly larger than that in Site A, while their maximum SSCs (4.17 kg/m^3 and 3.34 kg/m^3, respectively) were dramatically larger than that in Site A (3.28 kg/m^3) during the moderate wave conditions (Figs. 5 a-3, b-1, 7c). Therefore, as far as the larger SSF in Site A is concerned, it is the larger u resulting from strong undertow induced by breaking wave and radiation stresses decay in the surf zone that resulted in the larger net cross-shore suspended sediment flux at Site A. Though the strong fluid velocity accelerations under the steep leading face of the asymmetric waves enhance the sediment

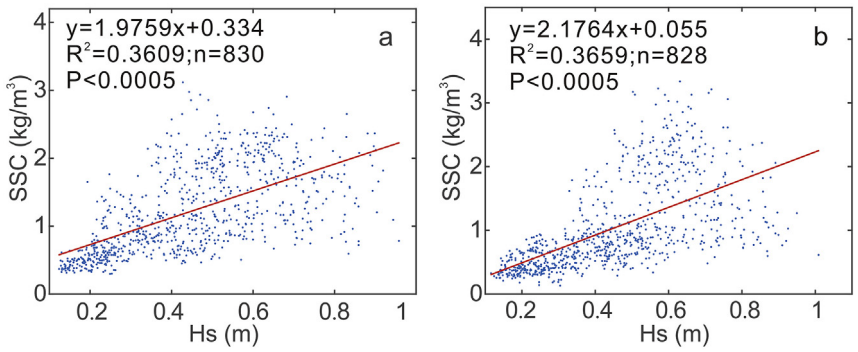

Fig. 11. Significant wave heights against suspended sediment concentrations in (a) Site B and (b) Site C.

entrainment and lead to the high SSC near the seabed (relative wave height is approaching to 0.78), the high turbidity signals may not reach the height of the OBS probe (more than 20 cm above the seabed) and could not be recorded.

5. Conclusions

Variations in near-bed cross-shore SST are not only a fundamental factor determining the amount of sediment discharged from nearshore to surf zone, but also a representation of erosion/accretion dynamics along beaches. Here, we show variations in sediment suspension and cross-shore SST from a field experiment over nearly six tidal cycles under the influence of two different wave conditions and tidal asymmetry at Yintan Beach, a meso-macro-tidal beach in China. The following conclusions are made from the study:

(1) During low-energy wave conditions, offshore-directed net cross-shore suspended sediment fluxes were several times smaller than that under moderate wave conditions at the meso-macro tidal Yintan Beach. The SSCs induced by different wave heights, rather than u in the water column, were responsible for variations in cross-shore suspended sediment fluxes under different wave conditions.
(2) Under moderate wave conditions, $< F >$ over the entire tidal cycle was dominated by a larger SSC and a longer flood tide duration during rising tide. The mean u values were in offshore direction for both flood and ebb tide except the flood tide of T24. During the flood tide of T24, H_s increased and the beach was highly dissipative. Massive suspended sediments were stirred by infra-gravity waves and transported by onshore-directed mean flows, which therefore led to abnormal onshore (positive) sediment transport.
(3) At the most landward measurement site, both $< F >$ and maximum cross-shore suspended sediment fluxes were larger than those in the offshore measurement sites over moderate wave conditions, which was ascribed to the strong offshore flows (undertow) induced by breaking waves, as well as radiation stress S_{xx} decay.

Acknowledgments

This study was supported by the National Natural Science Foundation of China (NSFC) (41666003; 41866001; 41376097). We are grateful to the editor and two anonymous reviewers for their constructive comments and suggestions that improved the article. All data in this study can access through corresponding author by email.

Appendix A. Supplementary data

Supplementary data to this article can be found online at https://doi.org/10.1016/j.ecss.2018.11.007.

References

Aagaard, T., Black, K.P., Greenwood, B., 2002. Cross-shore suspended sediment transport in the surf zone: a field-based parameterization. Mar. Geol. 185 (3), 283–302.
Aagaard, T., Greenwood, B., 1995. Suspended sediment transport and morphological response on a dissipative beach. Continent. Shelf Res. 15 (9), 1061–1086.
Aagaard, T., Hughes, M., Baldock, T., Greenwood, B., Kroon, A., Power, H., 2012. Sediment transport processes and morphodynamics on a reflective beach under storm and non-storm conditions. Mar. Geol. 326–328 (4), 154–165.
Aagaard, T., Hughes, M., Møller-sørensen, R., Anderson, S., 2006. Hydrodynamics and sediment fluxes across an onshore migrating intertidal bar. J. Coast Res. 22 (22), 247–259.
Aagaard, T., Nielsen, J., Greenwood, B., 1998. Suspended sediment transport and nearshore bar formation on a shallow intermediate-state beach. Mar. Geol. 148 (3–4), 203–225.
Almar, R., Castelle, B., Ruessink, B.G., Sénéchal, N., Bonneton, P., Marieu, V., 2010. Two- and three-dimensional double-sandbar system behaviour under intense wave forcing and a meso–macro tidal range. Continent. Shelf Res. 30 (7), 781–792.
Angnuureng, D.B., Almar, R., Senechal, N., Castelle, B., Addo, K.A., Marieu, V., Ranasinghe, R., 2017. Shoreline resilience to individual storms and storm clusters on a meso-macrotidal, barred beach. Geomorphology 290.
Anthony, E.J., Levoy, F., Monfort, O., 2004. Morphodynamics of intertidal bars on a megatidal beach, Merlimont, Northern France. Mar. Geol. 1 (1), 73–100.
Austin, M., Masselink, G., O'Hare, T., Russell, P., 2009. Onshore sediment transport on a sandy beach under varied wave conditions: flow velocity skewness, wave asymmetry or bed ventilation? Mar. Geol. 259 (1–4), 86–101.
Beach, R.A., Sternberg, R.W., 1988. Suspended sediment transport in the surf zone: response to cross-shore infragravity motion. Mar. Geol. 80 (1–2), 61–79.
Beach, R.A., Sternberg, R.,W., 1992. Suspended sediment transport in the surf zone: response to incident wave and longshore current interaction. Mar. Geol. 108 (3–4), 275–294.
Bird, E.C.F., 1985. Coastline Changes. Wiley & Sons, New York, pp. 219.
Bolaños, R., Thorne, P.D., Wolf, J., 2012. Comparison of measurements and models of bed stress, bedforms and suspended sediments under combined currents and waves. Coast. Eng. 62 (4), 19–30.
Boyd, R., Forbes, D.L., Heffler, D.E., 1988. Time-sequence observations of wave-formed sand ripples on an ocean shoreface. Sedimentology 35, 449–464.
Bruneau, N., Bertin, X., Castelle, B., Bonneton, P., 2014. Tide-induced flow signature in rip currents on a meso-macrotidal beach. Ocean Model. 74 (2), 53–59.
Butt, T., Russell, P., 1999. Suspended sediment transport mechanisms in high-energy swash. Mar. Geol. 161 (2–4), 361–375.
Cartier, A., Héquette, A., 2015. Vertical distribution of longshore sediment transport on barred macrotidal beaches, northern France. Continent. Shelf Res. 93, 1–16.
Capo, S., Parisot, J.P., Bujan, S., Senechal, N., 2009. Short time morphodynamics response of the Truc Vert Beach to storm conditions. J. Coast Res. 56 (2), 1741–1745.
Castelle, B., Bonneton, P., Dupuis, H., Senechal, N., 2007. Double bar beach dynamics on the high-energy meso-macrotidal French Aquitanian Coast: a review. Mar. Geol. 245 (1–4), 141–159.
Certain, R., Meulé, S., Rey, V., Pinazoet, C., 2017. Wave transformation on a microtidal barred beach (Sète, France). J. Mar. Syst. 58 (1), 19–34.
Conley, D.C., Beach, R.A., 2003. Cross-shore sediment transport partitioning in the nearshore during a storm event. J. Geophys. Res. Oceans 108 (C3), 103–133.
Cook, T.L., Sommerfield, C.K., Wong, K.C., 2007. Observations of tidal and springtime sediment transport in the upper Delaware Estuary. Estuar. Coast Shelf Sci. 72 (1–2), 235–246.
Dai, Z.J., Du, J.Z., Li, C.C., Chen, Z.S., 2007. The configuration of equilibrium beach profile in South China. Geomorphology 86 (3), 441–454.
Dai, Z.J., Li, C.C., Zhang, Q.L., 2004. Fractal analysis of shoreline patterns for crenulate bay beaches. Southern China, Estuar, Coast Shelf Sci. 61, 65–71.
Dai, Z.J., Liu, J.T., Lei, Y.P., Zhang, X.L., 2010. Patterns of sediment transport pathways on a headland bay beach-Nanwan beach, South China: a case study. J. Coast Res. 26 (6), 1096–1103.
Davis, R.A., 1972. Comparison of ridge and runnel systems in tidal and non-tidal environments. J. Sediment. Petrol. 42 (2), 413–421.
Delgado, R., Montreuil, A.L., Dan, S., Chen, M.S., 2015. Contribution of waves and currents to observed suspended sediment distribution patterns in a macro-tidal beach. Critical Readings in Planning Theory 81 (10), 147–173.
Elgar, S., Guza, R.T., 1985. Observations of bispectra of shoaling surface gravity waves. J. Fluid Mech. 161, 425–448.
Elgar, S., Gallagher, E.L., Guza, R.T., 2001. Nearshore sandbar migration. J. Geophys. Res. Atmos. 106 (106), 11623–11628.
Elgar, S., Herbers, T.H.C., Okihiro, M., Oltman-Shay, J., Guza, R.T., 1992. Observations of infragravity waves. J. Geophys. Res. Atmos. 97 (C10), 15573–15577.
Fang, G., Ichiye, T., 1983. On the vertical structure of tidal currents in a homogeneous sea. Geophys. J. Roy. Astron. Soc. 73, 65–82.
Fredsoe, J., Deigaard, R., 1992. Mechanics of coastal sediment transport. (Advanced Series in Ocean Engineering, vol. 3. World Scientific, Singapore, pp. 369.
Gallagher, E.L., Steve, E., Guza, R.T., 1998. Observations of sand bar evolution on a natural beach. J. Geophys. Res. Oceans 103 (C2), 3203–3215.
Ge, Z., Dai, Z., Pang, W., Li, S., Wei, W., Mei, X., Huang, H., Gu, J., 2017. Lidar-based detection of the post-typhoon recovery of a meso-macro-tidal beach in the Beibu Gulf, China. Mar. Geol. 391.
Grasso, F., Michalle, H., Barthélemy, E., 2011. Sediment transport associated with morphological beach changes forced by irregular asymmetric, skewed waves. J. Geophys. Res. Atmos. 116 (C3), 149–159.
Greenwood, B., Osborne, P.D., 1990. Vertical and horizontal structure in cross-shore flows: an example of undertow and wave set-up on a barred beach. Coast. Eng. 14 (6), 543–580.
Hanes, D.M., Huntley, D.A., 1986. Continuous measurements of suspended sand concentration in a wave dominated nearshore environment. Continent. Shelf Res. 6 (4), 585–596.
Harley, M.D., Turner, I.L., Kinsela, M.A., Middleton, J.H., Mumford, P.J., Splinter, K.D., Phillips, M.S., Simmons, J.A., Hansow, D.J., Short, A.D., 2017. Extreme coastal erosion enhanced by anomalous extratropical storm wave direction. Sci. Rep-UK. 7 (1), 6033.
Huang, H., Dai, Z.J., Shi, W.Y., Sheng, K., 2011. Deposition characteristics of beach profile in strong-tidal environment − A case study of Yintan, Guangxi during spring. Journal of Tropical Oceanography 30 (4), 71–76.
Jaffe, B.E., Sternberg, R.,W., Sallenger, A.H., 1984. The role of suspended sediment in shore-normal beach profile changes. In: Proceedings Coastal Engineering Conference. ASCE press, Houston, Texas, pp. 1983–1996.
Knutson, T.R., McBrige, J.L., Chan, J., Emanuel, K., Holland, G., Landsea, C., Held, I., Kossin, J.P., Srivastava, A.K., Sugi, M., 2010. Tropical cyclones and climate change. Nat. Geosci. 3, 157–163.
Kularatne, S., Pattiaratchi, C., 2008. Turbulent kinetic energy and sediment resuspension due to wave groups. Continent. Shelf Res. 28 (6), 726–736.
Kularatne, S., Pattiaratchi, C., 2014. The role of infragravity waves in near-bed cross-

shore sediment flux in the breaker zone. J. Mar. Sci. Eng. 2 (2), 568–592.
Longuet-Higgins, M.S., Stewart, R.W., 1964. Radiation stresses in water waves; a physical discussion, with applications. Deep-Sea Res. PT. I. 11 (4), 529–562.
Masselink, G., Auger, N., Russell, P., O'Hare, T.J., 2007a. Short-term morphological change and sediment dynamics in the intertidal zone of a macrotidal beach. Sedimentology 54 (1), 39–53.
Masselink, G., Austin, M., Tinker, J., O'Hare, T.J., Russell, P.E., 2008. Cross-shore sediment transport and morphological response on a macrotidal beach with intertidal bar morphology, Truc Vert, France. Mar. Geol. 251 (3–4), 141–155.
Masselink, G., Austin, M.J., O'Hare, T.J., Russell, P.E., 2007b. Geometry and dynamics of wave ripples in the nearshore zone of a coarse sandy beach. J. Geophys. Res. Atmos. 112 (C10) 275-275.
Masselink, G., Kroon, A., Davidson-Arnott, R.G.D., 2006. Morphodynamics of intertidal bars in wave-dominated coastal settings — a review. Geomorphology 73 (1–2), 33–49.
Masselink, G., Pattiaratchi, C., 2000. Tidal asymmetry in sediment resuspension on a macrotidal beach in northwestern Australia. Mar. Geol. 163 (1), 257–274.
Masselink, G., Russell, P., 2006. Flow velocities, sediment transport and morphological change in the swash zone of two contrasting beaches. Mar. Geol. 227 (3), 227–240.
Miles, J., Thorpe, A., 2015. Bedform contributions to cross-shore sediment transport on a dissipative beach. Coast. Eng. 98, 65–77.
Nielsen, P., 1981. Dynamics and geometry of wave-generated ripples. J. Geophys. Res. Atmos. 86 (C7), 6467–6472.
Nielsen, P., 1992. Coastal Bottom Boundary Layers and Sediment Transport. World Scientific.
Ogston, A.S., Sternberg, R.W., 1995. On the importance of nearbed sediment flux measurements for estimating sediment transport in the surf zone. Continent. Shelf Res. 15 (15), 1515–1524.
Osborne, P.D., Greenwood, B., 1992b. Frequency dependent cross-shore suspended sediment transport. 2. A barred shoreface. Mar. Geol. 106 (1–2), 25–51.
Osborne, P.D., Greenwood, B., 1992a. Frequency dependent cross-shore suspended sediment transport. 1. A nonbarred shoreface. Mar. Geol. 106, 1–24.
Osborne, P.D., Greenwood, B., 1993. Sediment suspension under waves and currents: time scales and vertical structure. Sedimentology 40 (4), 599–622.
Pan, S., Fairbairn, G., 2016. Impacts of submerged breakwaters on nearshore sediment transport. J. Coast Res. 1212–1216.
Paphitis, D., Collins, M.B., 2005. Sediment resuspension events within the (microtidal) coastal waters of Thermaikos Gulf, northern Greece. Continent. Shelf Res. 25 (19–20), 2350–2365.
Pereira, L.C.C., Vilaconcejo, A., Short, A.D., 2013. Influence of subtidal sand banks on tidal modulation of waves and beach morphology in Amazon macrotidal beaches. J. Coastal Res. Si (3), 1821–1826.
Pereira, L.C.C., Pinto, K.S.T., Vila-Concejo, A., 2014. Morphodynamic variations of a macrotidal beach (atalaia) on the Brazilian amazon coast. J. Coast Res. 681–686.
Poate, T., Masselink, G., Russell, P., Austin, M., 2014. Morphodynamic variability of high-energy macrotidal beaches, Cornwall, UK. Mar. Geol. 350 (4), 97–111.
Puleo, J.A., Beach, R.A., Holman, R.A., Allen, J.S., 2000. Swash zone sediment suspension and transport and the importance of bore-generated turbulence. J. Geophys. Res. Oceans 105 (7), 17021–17044.
Reichmüth, B., Anthony, E.J., 2007. Tidal influence on the intertidal bar morphology of two contrasting macrotidal beaches. Geomorphology 90 (1–2), 101–114.
Ridderinkhof, H., Ham, R.V.D., Lee, W.V.D., 2000. Temporal variations in concentration and transport of suspended sediments in a channel–flat system in the Ems-Dollard estuary. Continent. Shelf Res. 20 (12–13), 1479–1493.
Roelvink, J.A., Stive, M.J.F., 1989. Bar-generating cross-shore flow mechanisms on a beach. J. Geophys. Res. Atmos. 94 (C4), 4785–4800.
Russell, P., Davidson, M., Huntley, D., Hardisty, J., Cramp, A., 1991. The British beach and nearshore dynamics (B-Band) programme. Proceedings Coastal Sediments '91. ASCE press, Seattle, Washington, D. C., pp. 371–384.
Sherman, D.J., Greenwood, B., 1984. Boundary roughness and bedforms in the surf zone. Mar. Geol. 60 (1–4), 199–218.
Simmons, H.B., 1955. Some effects of upland discharge on estuarine hydraulics. Proc. Am. Soc. Civ. Eng. 81 (792), 1–20.
Soulsby, R., 1997. Dynamics of Marine Sands: a Manual for Practical Applications. Thomas Thelford, London, UK.
Stive, M.J.F., Reniers, A.J.H.M., 2003. Sandbars in motion. Science 299 (5614), 1855–1856.
Sunamura, T., Takeda, I., 1984. Landward migration of inner bars. Mar. Geol. 60 (1–4), 63–78.
Sutherland, T.F., Lane, P.M., Amos, C.L., Downing, J., 2000. The calibration of optical backscatter sensors for suspended sediment of varying darkness levels. Mar. Geol. 162 (2–4), 587–597.
Swart, D.H., 1974. A schematisation of onshore-offshore transport. Proc. 14th Int. Conf. Coast. Eng. ASCE 1782–1798.
Thornton, E.B., Humiston, R.T., Birkemeier, W., 1996. Bar/trough generation on a natural beach. J. Geophys. Res. Atmos. 101 (101), 12097–12110.
Uday, P., Svendsen, I.A., 2012. Vertical structure of the undertow outside the surf zone. J. Geophys. Res. Oceans. 98 (C12), 22707–22716.
van Rijn, L.C., 1993. Principles of Sediment Transport in Rivers, Estuaries and Coastal Seas. Aqua Publication, Amsterdam, the Netherlands, pp. 2.2–2.4 (pp. 2.7; pp. 2.15-2.16).
Wang, Y.P., Voulgaris, G., Li, Y., Yang, Y., Chen, J., Gao, S., 2013. Sediment resuspension, flocculation, and settling in a macrotidal estuary. J. Geophys. Res. Oceans 118 (10), 5591–5608.
Wells, D.R., 1967. Beach equilibrium and second-order wave theory. J. Geophys. Res. Atmos. 72 (2), 497–504.
Wesselman, D., Winter, R.D., Engelstad, A., McCall, R., Dongeren, A.V., Hoekstra, P., Oost, A., Vegt, M.V.D., 2017. The effect of tides and storms on the sediment transport across a Dutch barrier island. Earth Surf. Process. Landforms.
Xia, H., Xia, Z., Zhu, L., 2004. Vertical variation in radiation stress and wave-induced current. Coast. Eng. 51 (4), 309–321.
Zhou, G., Huang, J., Tao, Y., Luo, Q., Zhang, G., 2015. Temporal-spatial distribution of wave energy: a case study of Beibu Gulf, China. Renew. Energy 74, 344–356.